Resonant Beam Communications With Echo Interference Elimination

Mingliang Xiong, Qingwen Liu, *Senior Member, IEEE*, Gang Wang, *Member, IEEE*, Georgios B. Giannakis, *Fellow, IEEE*, Sihai Zhang, *Senior Member, IEEE*, Jinkang Zhu, *Life Member, IEEE*, and Chuan Huang, *Member, IEEE*

***Abstract*—Resonant beam communications (RBCom) is capable of providing wide bandwidth when using light as the carrier. Besides, the RBCom system possesses the characteristics of mobility, high signal-to-noise ratio (SNR), and multiplexing. Nevertheless, the channel of the RBCom system is distinct from other light communication technologies due to the echo interference issue. In this article, we reveal the mechanism of the echo interference and propose the method to eliminate the interference. Moreover, we present an exemplary design based on frequency shifting and optical filtering, along with its mathematic model and performance analysis. The numerical evaluation shows that the channel capacity is greater than 15 b/s/Hz.**

***Index Terms*—Frequency-shift filtering, Internet of Things, laser communications, optical mobile communications (OMC), resonant beam system (RBS).**

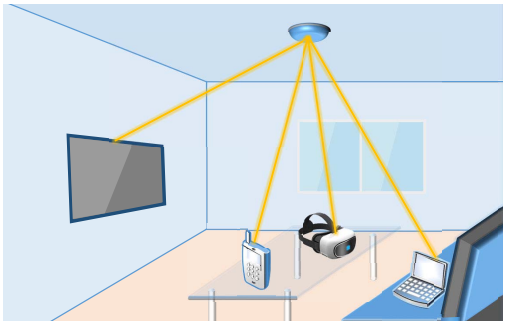

Fig. 1. Scenario of RBCom.

I. Introduction

THE RAPID advancement of mobile communications has been along with the increased carrier frequency. According to Shannon's law, wider bandwidth supports higher channel capacity. Therefore, the sixth generation (6G) mobile communications is expected to operate at terahertz [2]–[5].

Wireless optical communications (WOC) that uses infrared or visible light is a promising technology, as its carrier frequency is up to several hundred terahertz [6]. Light-emitting diodes (LEDs) and lasers are the most common light emitters employed in WOC [7], [8]. Depending on the functionality, they can be categorized into non-line-of-sight (NLOS) and line-of-sight (LOS) WOC [9]. The former is based on the diffuse reflection of ceilings and walls, leading to low received power and low signal-to-noise ratio (SNR).

Most LOS WOC transmitters focus their LED radiation or laser beams on the receiver to obtain a high-level SNR. However, it is generally difficult for these directional transmitters to track the receiver. Microelectromechanical system (MEMS)-actuated beam steering employed in many research exhibit a slow response for tracking [10], [11].

Employing nonmechanical beam steering, some optical mobile communication (OMC) systems can response with a high speed and accuracy. For example, some research employs static diffraction gratings for fast beam steering [12]. The direction of the beam is controlled through changing the beam wavelength. Besides, a 2-D multiple-beam steering is implemented with a pair of crossed gratings as well as a multiple-wavelength beam. An alternative beam steering relies on spatial light modulators (SLMs) [13]. Each pixel of the SLM plane can be controlled to change the phase of the light that passes through this pixel. A complex light field containing multiple beams can be generated by the SLM for point-to-multipoint communication. These technologies need high-accuracy localization. However, radio frequency (RF) for localization usually undergoes electromagnetic interference (EMI) [14].

Resonant beam communications (RBCom) has the capability of high SNR, mobility, and multiplexing. The transmitter can generate resonant beams to receivers automatically,

Manuscript received May 9, 2020; revised August 5, 2020; accepted August 28, 2020. Date of publication September 1, 2020; date of current version February 4, 2021. The work of Mingliang Xiong and Qingwen Liu was supported by the National Natural Science Foundation of China under Grant 61771344. The work of Gang Wang was supported by the National Natural Science Foundation of China under Grant 61720106011, Grant 61925303, and Grant U1613225. The work of Georgios B. Giannakis was supported by the National Science Foundation under Grant 1711471 and Grant 1901134. This article was presented in part at the 11th International Conference on Wireless Communications and Signal Processing (WCSP), Xi'an, China, October 23–25, 2019. *(Corresponding author: Qingwen Liu.)*

Mingliang Xiong and Qingwen Liu are with the College of Electronics and Information Engineering, Tongji University, Shanghai 201804, China (e-mail: xiongml@tongji.edu.cn; qliu@tongji.edu.cn).

Gang Wang is with the State Key Laboratory of Intelligent Control and Decision of Complex Systems and the School of Automation, Beijing Institute of Technology, Beijing 100081, China (e-mail: gangwang@bit.edu.cn).

Georgios B. Giannakis is with the Department of Electrical and Computer Engineering, University of Minnesota, Minneapolis, MN 55455 USA (e-mail: georgios@umn.edu).

Sihai Zhang and Jinkang Zhu are with the Key Laboratory of Wireless-Optical Communications, University of Science and Technology of China, Hefei 230026, China (e-mail: shzhang@ustc.edu.cn; jkzhu@ustc.edu.cn).

Chuan Huang is with the School of Science and Engineering, Chinese University of Hong Kong, Shenzhen 518172, China (e-mail: huangchuan@cuhk.edu.cn).

Digital Object Identifier 10.1109/JIOT.2020.3020908

without a software or hardware controller, as depicted in Fig. 1. The frequency of the resonant beam is up to 282 THz.

Resonant beam system (RBS) is the core structure of the RBCom system, and it features self-alignment, high power, and multiple beams (see [1], [15]–[17]). RBS is suitable for scenarios where high-power and long-distance power transmission are required, which is different from RF-based power harvesting technologies [18]–[21]. In RBS, a spatially separated laser resonant cavity is formed by the transmitter and the receiver [22], [23]. In this cavity, the resonant beam oscillating back and forth acts as the transmission carrier. With the retroreflectors at both transmitter and receiver, the RBCom transmitter is capable of tracking receivers automatically. However, it also results in echo interference.

In this article, we elaborate on the mechanism of echo interference in the RBCom system and reveal the causes of the interference, including the reflected signal, the backward modulation, and the gain fluctuation. Afterward, we present the method of eliminating the echo interference and propose an exemplary design as well as its mathematic channel model.

The remainder of this article is organized as follows. In Section II, we present the mechanism of RBCom. In Section III, we analyze the causes of echo interference in the RBCom channel. In Section IV, we illustrate the echo interference elimination method based on frequency shifting and optical filtering. In Section V, we demonstrate the interference-free RBCom system design as well as the performance analysis. Finally, we make the conclusions in Section VI.

II. Resonant Beam Communications

Based on the RBS system, the RBCom transmitter sends resonant beams to multiple receivers. By modulating the resonant beams, high-SNR mobile communications can be achieved. The RBS cavity is an open laser cavity and we will describe the similarities as well as differences between it and traditional lasers in this section.

In a common laser cavity, photons oscillate between two aligned mirrors (a back mirror and a front mirror) and are amplified by the gain medium [24]. This optical amplification capability is supported by stimulated emission which is powered by the pump source (electricity or light). A small proportion of oscillating photons pass through the front mirror (transmittance is larger than 0) to yield a laser beam. Note that the two mirrors of the laser cavity have to be aligned accurately, otherwise, the oscillation cannot be maintained.

In Fig. 2(a), using two retroreflectors at both ends of the RBS, this design provides the capability of self-alignment, supporting the mobility of RBS. Retroreflectors can reflect the incident beam back along the incident direction [25], [26]. Therefore, there is a path for photon oscillating between two retroreflectors. The resonant beam is formed in this oscillating path regardless of the position and the attitude of the retroreflectors. The two retroreflectors are aligned automatically, so the intracavity resonant beams exist even when the receivers are moving.

In addition to the RBS structure, the RBCom system has some necessary optical components, including an electro-optic modulator (EOM), optical filter, and splitter. These components usually only operate at a fixed beam incidence angle, which can be satisfied by the cat's eye structure presented in [27]. Fig. 2(b) demonstrates a transmitter design based on the cat's eye structure. All the outside beams that pass the focal point of the lens L3 and enter the transmitter can be reflected to their source. In the body of this transmitter structure, two special zones satisfy the needs of the aforementioned optical components, i.e., between the mirror M1 and the lens L1, and between the lenses L2 and L3. Beams in these zones are parallel to the optical axis, so a fixed incident angle onto these optical components can be guaranteed. Moreover, other optical components can be integrated into the transmitter to take charge of operations, including the selection of transverse and longitudinal modes.

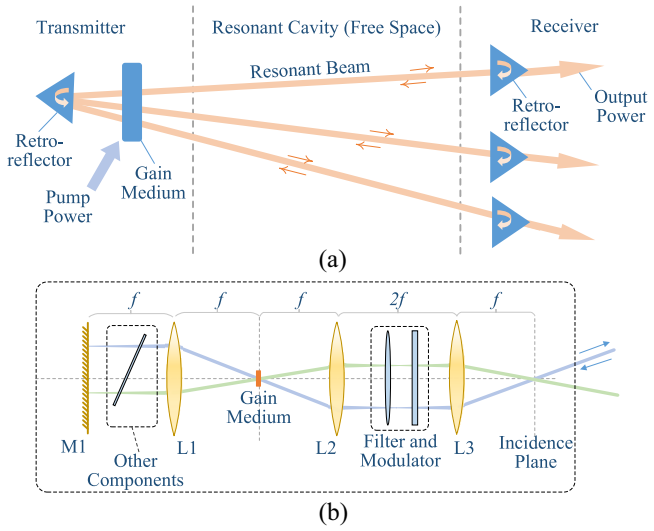

Fig. 2. RBS. (a) System structure. (b) Transmitter design based on the cat's eye structure.

Owing to the spatially separated resonant cavity, RBCom features safety, mobility, and multiplexing, which are elaborated as follows [28].

1) *High-SNR and Safe:* The pencil beam generated in the resonant cavity carries high-power optical energy to the receiver, enabling high-SNR communication. When foreign objects enter the beam path, the highest order transverse modes stop oscillating due to increased diffraction loss, and the power is transferred to lower order modes. With the deep entering of the foreign objects, lower order modes will vanish. As the lowest modes stop oscillating, the resonant beam ceases, ensuring safety.
2) *Mobility:* Due to the self-alignment capability of the retroreflector, a robust cavity can be created for forming a resonant beam even when the transmitter and the receiver change their positions. Hence, mobile communications can be enabled.
3) *Multiplexing:* One transmitter can be connected with multiple receivers. For each receiver, an individual resonant cavity is created within which a resonant beam is formed. This feature, cooperating with time-division multiplexing access (TDMA) scheme or SLM array, supports multiuser communications.

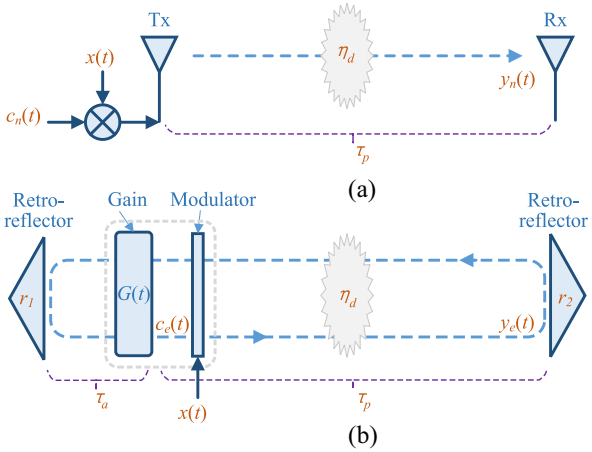

Fig. 3. Channel comparison of (a) nonecho case and (b) echo-interfered case.

The channel of the RBCom system is different from that of other communication systems. The carrier beam profile is determined by the resonating scheme, which means that the beam radius and the transverse intensity pattern are adjusted automatically to improve the transmission efficiency. Modulation is performed by the EOM located on the beam path. The electric field amplitude of the carrier beam is modulated during the modulation procedure. However, the retroreflector at the receiver reflects the signal back to the transmitter, affecting the modulation procedure, which is detailed in the next section.

III. Echo-Interfered Channel

In this section, the channel characteristics of RBCom are analyzed. Fig. 3(a) and (b) depicts a conventional nonecho communication channel and a RBCom channel, respectively. Both of them are used to transmit signals from the transmitter (the left-hand side) to the receiver (the right-hand side). Nevertheless, the RBCom channel undergoes echo interference, which makes it completely different from the nonecho channel.

In conventional communication systems, the channel does not exhibit echo interference. As shown in Fig. 3(a), the transmit antenna (Tx) sends the modulated signal to the receive antenna (Rx). The carrier signal $c_n(t)$ is monochromatic with the amplitude that is a constant. The source signal is $x(t)$. The modulated signal is the product of the carrier signal and the source signal.

In contrast, the channel of RBCom systems has echo interference. As shown in Fig. 3(b), the carrier beam in the resonant cavity is expressed as

$$c_e(t) = A_c(t)e^{i\omega_c t} \tag{1}$$

where $i \coloneqq \sqrt{-1}$, $A_c(t)$ is the amplitude, and ω_c is the beam frequency. Here, we assume a single-frequency carrier beam which can be obtained by adding mode-selecting components into the cavity. The modulated signal travels circularly in the cavity. In a single round trip, a proportion of the received signal is reflected back to the transmitter, constituting the echo signal. Then, the echo signal is changed by the modulator and amplified by the gain medium, respectively. Afterward, the transmitter's retroreflector reflects the echo to the gain medium. Finally, the echo reaches at the modulator, serving as the carrier. The echo will be modulated subsequently. Hence, the amplitude of the carrier is time variant; that is

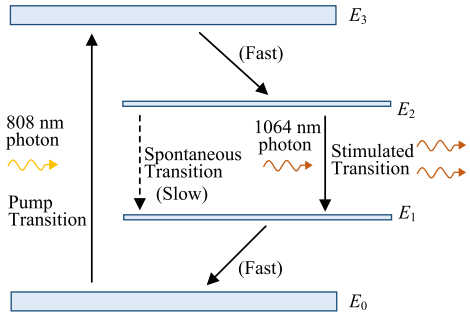

Fig. 4. Simplified energy-level diagram of a four-level system.

$$A_c(t) = r_1 r_2 \eta_d y_e\big(t - \tau_p - 2\tau_a\big)x(t - 2\tau_a)G(t - 2\tau_a)G(t) \tag{2}$$

where r_1 and r_2 are the retroreflectors' reflection coefficients (intensity reflectivity are r_1^2 and r_2^2); η_d is the transmission coefficient for the beam to travel from one side to another side of the cavity (in this article, the term *transmission coefficient* is used to describe the amplitude change ratio of a wave passing through an object, such as a mass of air or a lens); $G(t)$ is the time-variant gain provided by the gain medium; τ_p is the single-pass transmission time between the transmitter's modulator and the receiver; and τ_a is the time that signals travel from the retroreflector at the transmitter to the modulator. For simplicity, the thickness of the gain medium and the modulator is neglected. The interval between the medium and the modulator is also neglected. The cavity length is $L = (\tau_a + \tau_p)v$, where v is the light speed.

The modulated signal is the product of the carrier amplitude and the modulator's transparency. Hence, the amplitude of the received signal is

$$\begin{aligned} y_e(t) &= \eta_d x\big(t - \tau_p\big)A_c\big(t - \tau_p\big) \\ &= r_1 r_2 \eta_d^2 y_e\big(t - 2\tau_p - 2\tau_a\big)x\big(t - \tau_p - 2\tau_a\big) \\ &\quad \times G\big(t - \tau_p\big)G\big(t - \tau_p - 2\tau_a\big)x\big(t - \tau_p\big). \end{aligned} \tag{3}$$

The term $x(t - \tau_p)$ is the source signal to be transmitted. It is clear that the received signal is interfered by the following aspects. The first interference is the previous received signal, which is $y_e(t - 2\tau_p - 2\tau_a)$ in (3). The second interference is produced by the modulator, as the backwards echo coming from the receiver is also changed by the modulator. Thus, the echo is multiplied by $x(t - \tau_p - 2\tau_a)$. The last impact stems from the gain medium due to its time-varying gain. The echo is amplified twice through the gain medium. Hence, the echo is multiplied by $G(t - \tau_p)G(t - \tau_p - 2\tau_a)$.

The RBCom cavity is a time-variant system. So gain variation can be observed if there is any influence imposed on the intracavity resonant beam. As depicted in Fig. 4, the gain medium is often modeled as a four-level system with four energy levels $\{E_0, E_1, E_2, E_3\}$. As the pump light (e.g., 808 nm) enters the gain medium, the populations at E_0 transit to E_3 through stimulated absorption, and then quickly transit

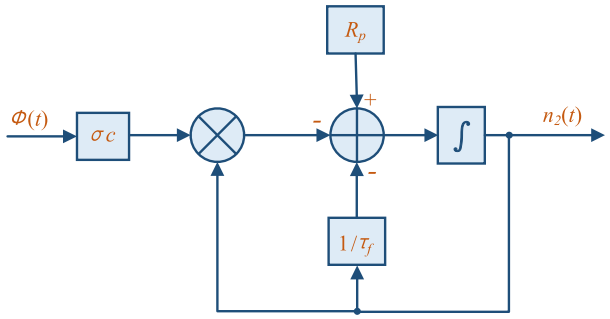

Fig. 5. Upper level population density interacting with photon density.

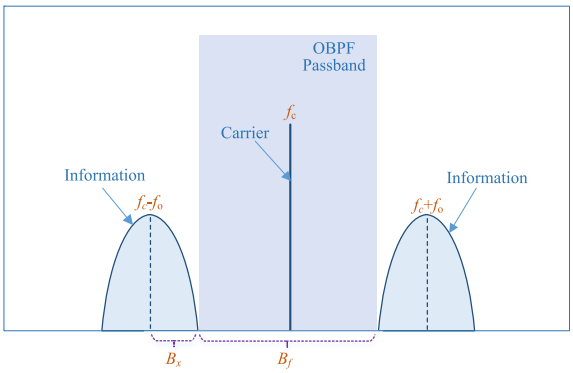

Fig. 6. Interference elimination with optical filtering.

to E_2. As the oscillating photons (e.g., 1064 nm) enter the gain medium, the populations at E_2 transit to E_1, generating extra 1064 nm photons through stimulated emission. Generally, the population densities at E_1 and E_3 are assumed to be 0, as the lifetime of the populations at energy level E_1 and E_3 is much shorter than that of populations at other energy levels [24]. Let n_0 (n_2) denote the density of populations at E_0 (E_2), the aforementioned phenomenon is described mathematically by the following simplified rate equations [24], [29]:

$$\frac{\partial n_2}{\partial t} = -n_2\phi\sigma v - \frac{n_2}{\tau_f} + R_p \tag{4}$$

$$\frac{\partial \phi}{\partial t} = n_2\phi\sigma v - \frac{\phi}{\tau_c} + S \tag{5}$$

where ϕ is the photon density; σ is the stimulated emission cross section; τ_f is the fluorescence lifetime; R_p is the pump rate depending on the pump power; τ_c is the photons lifetime; and S is the spontaneous emission rate for photons to be coupled into the cavity. Equations (4) and (5) describe the change rate of n_2 and ϕ, respectively.

Stimulated emission results in a decrease of n_2 and an increase of ϕ [24]. Simultaneously, the stimulated emission rate is also determined by n_2 and ϕ, as $n_2\phi\sigma v$ in (4) and (5) represents the stimulated emission rate. During this process, the populations at energy level E_2 decay to the ground level E_0 through generating an equivalent number of photons. The photons are consumed gradually, as there are air absorption and diffraction loss in the cavity. The density n_2 of populations at energy level E_2 is supplied by the stimulated absorption transition of the populations at E_0 with rate R_p, which is related to n_0 and the pump power P_{in}. Generally, if P_{in} is stable, R_p can be assumed as a constant, since $n_0 \gg n_2$. A negative-feedback mechanism can be observed in the rate equation system. Given adequate P_{in}, the rate equation system can reach the steady state, in which $\partial\phi/\partial t = \partial n_2/\partial t = 0$ [24]. A quasi-monochromatic resonant beam can be obtained when the system becomes stable. For simplicity, we assume the resonant beam at the steady state is a monochromatic wave.

The upper level population density n_2 determines the amplitude gain provided by the gain medium. This relationship is expressed as [24]

$$G(t) = \sqrt{e^{n_2(t)\sigma l}} \tag{6}$$

where l is the gain medium length. Fig. 5 depicts how ϕ affects n_2. Moreover, both $n_2(t)$ and $G(t)$ are nonlinear systems related to the pump rate R_p. Consequently, gain fluctuation exists when the pump source of the gain medium has a time-variant power.

In a nutshell, the RBCom channel is difficult to be utilized for communications directly. The following three issues need to be addressed for establishing a noninterference resonant beam channel.

1) *Reflected Signal:* The echo beam reflected by the receiver is composed of information components, affecting the subsequent modulation. The echo should not be cut off arbitrarily as it plays a key role in maintaining the resonance. An effective way to eliminate the information signal in the echo is to remove its components in the frequency domain.
2) *Backward Modulation:* Not only the forward beam is changed by the modulator, the reflected echo beam is also changed as it passes through the modulator. Even if the echo is pure with the only carrier frequency, other frequencies will be added to the echo when it passes through the modulator. The frequency components induced by the backward modulation need to be removed.
3) *Gain Fluctuation:* Only under a balance condition can the gain become stable, where the upper level population density as well as the photon density is no longer changed. Any impacts applied to the gain medium will result in gain fluctuation. Hence, the pump power as well as the stimulated photon density in the cavity should be a static value during the communication process.

IV. Interference Elimination

The RBCom channel undergoes echo interference, and therefore cannot be utilized directly for data transfer. Yet, it is able to eliminate the echo and create a well-performed noninterference channel. For this purpose, the information components in the echo should be removed; the impacts of the backward modulation should be avoided; and the gain stability should be maintained. Two procedures presented below are adopted to meet these requirements.

A. Optical Filtering

As demonstrated in Fig. 6, the desired spectrum pattern of the modulated signal should allow the information bands to

be completely filtered out, which is described as

$$Y(f) = p'C_0(f) + \frac{m'}{4}X(f+f_c+f_o) + \frac{m'}{4}X(f+f_c-f_o) + \frac{m'}{4}X(f-f_c+f_o) + \frac{m'}{4}X(f-f_c-f_o). \quad (7)$$

The modulated signal $Y(f)$ is composed of the information bands $X(f)$ and the carrier components $C_0(f)$. The carrier is a monochromatic wave with frequency of f_c as the resonance reaches stable. Thus, the carrier's frequency spectrum is

$$C_0(f) = \frac{1}{2}\delta(f-f_c) + \frac{1}{2}\delta(f+f_c) \quad (8)$$

where $\delta(f)$ denotes the unit-impulse function. As the positive and the negative frequency axis are symmetrical, Fig. 6 only demonstrates the positive axis. Two frequency bands carrying information sit symmetrically over f_c, at frequencies $f_c \pm f_o$, respectively.

The OBPF has a central frequency f_c and a bandwidth B_f. Hence, the frequency response of the OBPF is

$$H_{\mathrm{OBPF}}(f) = \Pi\left(\frac{f+f_c}{B_f}\right) + \Pi\left(\frac{f-f_c}{B_f}\right) \quad (9)$$

where $\Pi(f)$ is the rectangular function described as

$$\Pi(f) = \begin{cases} 1, & |f| \le 1/2 \\ 0, & |f| > 1/2. \end{cases} \quad (10)$$

The information bands can be removed only when they are out of the filter's passband. Hence, the following condition needs to be met; that is

$$0 < B_f < 2f_o - 2B_x \quad (11)$$

where B_x is the source signal bandwidth. After filtering, only carrier frequency exists in the echo, namely

$$Y'(f) = Y(f)H_{\mathrm{OBPF}}(f) = p'C_0(f). \quad (12)$$

According to (12), OBPFs detach the information components from the echo. The carrier frequency in the echo is preserved for maintaining the beam resonance. In this case, the previous transmitted information signal cannot interfere the ongoing modulation. In the same way, the impact of the backward modulation can be eliminated.

B. Maintaining Gain Stability

The power loss of the photons in the cavity is compensated by the gain medium. In order to generate a resonant beam, the gain of the gain medium must be greater than the total loss in the cavity at the beginning of the communication progress. On this premise, the photon density in the cavity increases gradually, which also speeds up the consumption of the populations at the energy level E_2 in the gain medium. In the meantime, the gain decreases gradually until becoming equal to the loss. Finally, the system achieves a steady state where the gain as well as the upper level population density n_2 will not change. This process is based on the negative-feedback mechanism of the gain system.

During the modulation, the gain system has to be kept in the steady state, for which two requirements introduced in the following should be satisfied.

1) *Steady Photon Density in Gain Medium:* In Fig. 5, the steady state of the gain system will be broken when meeting photon density fluctuation. In this case, the gain is unexpectedly dynamic. Consequently, the echo toward the gain medium is expected to have a constant intensity (i.e., a constant photon density). As depicted in (12), a monochromatic wave that has constant amplitude and constant intensity is obtained.
2) *Threshold Condition:* During each round trip, the gain is required to be greater than the loss; otherwise, the resonance cannot be built up [24]. Hence, the round-trip transmission coefficient $\mathcal{G}_r$ must satisfy

$$\mathcal{G}_r(t) = \frac{c'_e(t)}{c'_e\big(t-2\tau_a-2\tau_p\big)} = r_1 r_2 \eta_m^2 \eta_d^2 G^2(t) \ge 1 \quad (13)$$

where η_m is the transmission coefficient of the modulator which is determined by the operating point; and $c'_e(t)$ is the carrier processed by OBPFs. We assume the OBPF is an ideal device, so the attenuation in the passband is neglected. The steady state where $\mathcal{G}_r(t) = 1$ is obtained automatically because of the negative-feedback mechanism mentioned above. Then, the steady-state gain is given as follows:

$$G = G(t)\Big|_{\mathcal{G}_r(t)=1} = \frac{1}{\eta_m \eta_d \sqrt{r_1 r_2}}. \quad (14)$$

V. Exemplary Design

In the above section, two procedures are proposed for interference elimination, i.e., optical filtering and gain stability maintenance. These interference-eliminating procedures are demonstrated next with an exemplary system design.

As shown in Fig. 7, before entering the electro-optic amplitude modulator, the source signal $mx(t)$ (the amplitude $m \ge 0$ and $|x(t)| \le 1$) is preprocessed for meeting the desired spectrum pattern. At the receiver, a splitter is used to reflect a fraction of the resonant beam to the photon detector (PD) for demodulation, and the rest of the beam that passes through the splitter is reflected back to the transmitter by a retroreflector for maintaining the resonance. The OBPF behind the splitter is adopted to detach the information bands from the echo's spectrum. Between the gain medium and the modulator, another OBPF is mounted to detach the undesired frequency generated through backward modulation. Modulation, demodulation, and gain stability maintenance are detailed as follows.

A. Modulation

In order to ensure that the source signal band is away from zero frequency, the band of the source signal should be shifted by $\omega_o/2\pi$. According to Fig. 7, the local oscillation $\cos\omega_o t$ and the source signal $mx(t)$ is mixed up by a mixer to conduct frequency shifting. Next, the operating point for the modulator is specified by adding a direct-current (DC) bias p to the processed signal.

When the RBCom achieves the steady state where the carrier amplitude A_c is a constant, the modulation is able to be initiated. Then, the field of the carrier beam is depicted as

$$E_c(t) = \mathrm{Re}\big[A_c e^{i\omega_c t}\big] \quad (15)$$

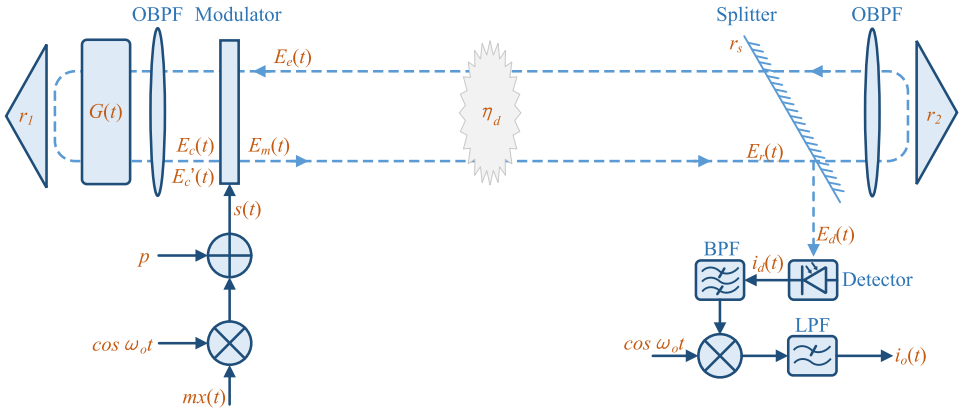

Fig. 7. Exemplary resonant beam communication system design with echo elimination.

where ω_c represents the angular frequency, and $\mathrm{Re}[\cdot]$ takes the real part. Hence, the modulated beam's field is expressed as

$$E_m(t) = \big[mx(t)\cos\omega_o t + p\big]E_c(t) \tag{16}$$

where $0 < p - m$ and $p + m < 1$; and both p and m are defined as positive values. To give full play to the modulator's performance, we choose $p+m = 1$, thus, the modulation depth m is constrained by operating point p.

The modulated beam experiences amplitude attenuation with ratio $\eta_d = \eta_{\text{diff}} \exp(-\alpha d/2)$ as transferred from the transmitter to the receiver, where η_{diff} is the amplitude attenuation ratio induced by diffraction loss, α is the loss coefficient of atmosphere (for different air conditions, including clear air, haze, and fog, α are 0.0001, 0.001, and 0.01 m^{-1}, respectively) [30], and d is the transmission distance. Hence, the received electric field at the receiver's splitter is

$$E_r(t) = \eta_d E_m(t). \tag{17}$$

B. Demodulation

At the receiver, a fraction of the received beam is reflected to the PD by the splitter. Here, r_s denotes the splitter's reflection coefficient. The electric field at the PD is

$$\begin{aligned} E_d(t) &= r_s E_r(t) \\ &= \mathrm{Re}\big[\tilde{E}_d(t)\big] \end{aligned} \tag{18}$$

where

$$\tilde{E}_d(t) = r_s \eta_d A_c \big[mx(t)\cos\omega_o t + p\big] e^{i\omega_c t}. \tag{19}$$

The PD converts the incident beam to photocurrent. According to [31], the generated photocurrent is proportional to the intensity of the incident light

$$i_d(t) \propto \tilde{E}_d(t)\tilde{E}_d^*(t) \tag{20}$$

where $\tilde{E}_d^*(t)$ is the complex conjugate of $\tilde{E}_d(t)$. Consequently, the current signal generated by the PD is

$$\begin{aligned} i_d(t) &= k\big\{r_s \eta_d A_c \big[mx(t)\cos\omega_o t + p\big]\big\}^2 + n(t) \\ &= \frac{1}{2} k r_s^2 \eta_d^2 A_c^2 m^2 x^2(t)\cos 2\omega_o t \\ &\quad + 2k r_s^2 \eta_d^2 A_c^2 p m x(t)\cos\omega_o t \\ &\quad + \frac{1}{2} k r_s^2 \eta_d^2 A_c^2 m^2 x^2(t) \\ &\quad + k r_s^2 \eta_d^2 A_c^2 p^2 + n(t) \end{aligned} \tag{21}$$

where $k = \eta_{\text{det}} \rho \mathcal{A}_b / Z_0$ is a constant; ρ is PD's responsivity; $\mathcal{A}_b$ is the cross section area of the beam; $Z_0 \approx 377\ \Omega$ is the impedance of free space; $n(t)$ is the PD's additive Gaussian white noise (AWGN); and η_{det} is the ratio of the detected power to the total incident beam power. The average photocurrent I_{sig} contributes to the shot noise of the PD. From (21), we can obtain

$$I_{\text{sig}} = k r_s^2 \eta_d^2 A_c^2 p^2 + \frac{1}{2} k r_s^2 \eta_d^2 A_c^2 m^2 \left\langle x^2(t) \right\rangle \tag{22}$$

where $< \cdot >$ is the expectation operation.

The frequency band of the first three terms on the right-hand side of (21) are $[2f_o - 2B_x, 2f_o + 2B_x]$, $[f_o - B_x, f_o + B_x]$, and $[-2B_x, 2B_x]$, respectively, where B_x is the bandwidth of $x(t)$. The local oscillation frequency is $f_o = \omega_o/2\pi$. Since the source signal $x(t)$ is contained in the second term, a bandpass filter (BPF) with bandwidth of $2B_x$ is employed to extract the second term. For this purpose, the frequency band of the second term should not overlap with the frequency bands of others. Therefore, the following restriction has to be satisfied:

$$\begin{cases} f_o + B_x < 2f_o - 2B_x \\ f_o - B_x > 2B_x \end{cases} \Rightarrow f_o > 3B_x. \tag{23}$$

Next, coherent demodulation scheme is adopted. The extracted term is mixed with $\cos\omega_o t$ and then processed by a low-pass filter (LPF) whose bandwidth is B_x to obtain the low-frequency band. Thus, the demodulated signal is

$$i_o(t) = k r_s^2 \eta_d^2 A_c^2 p m x(t) + \frac{1}{2} n_b(t) \tag{24}$$

where $n_b(t)$ is the band-limited white noise.

C. Optical Filtering

As demonstrated in Fig. 7, the beam passes through the OBPF twice at the receiver. The received electric field at the splitter is

$$\begin{aligned} E_r(t) &= \frac{1}{2}\eta_d A_c m x(t)\cos(\omega_c - \omega_o)t \\ &\quad + \frac{1}{2}\eta_d A_c m x(t)\cos(\omega_c + \omega_o)t \\ &\quad + p\eta_d A_c \cos\omega_c t. \end{aligned} \tag{25}$$

The spectrum of $E_r(t)$ meets the pattern depicted by (7). The echo field that goes into the modulator is obtained as

$$\begin{aligned} E_e(t) &= r_2 t_s \eta_d E_r(t) * h_{\mathrm{OBPF}}(t) * h_{\mathrm{OBPF}}(t) \\ &= r_2 t_s p \eta_d^2 A_c \cos \omega_c t \end{aligned} \tag{26}$$

where $t_s = \sqrt{1 - r_s^2}$ is the splitter's transmission coefficient, and $h_{\mathrm{OBPF}}(t)$ is the OBPF's impulse response. As depicted by (26), a monochromatic beam is obtained.

The light wave arrives at the modulator after one round trip and can be represented as

$$\begin{aligned} E_c'(t) &= E_e(t) s(t) * h_{\mathrm{OBPF}}(t) G^2 * h_{\mathrm{OBPF}}(t) \\ &= r_1 r_2 t_s p^2 \eta_d^2 G^2 A_c \cos \omega_c t \end{aligned} \tag{27}$$

where G is the cavity gain at the steady state defined in (14). From (27), $E_c'(t)$ is independent of $x(t)$, which means the interference induced by the reflected signal is eliminated.

D. Gain Stability

The gain stability is not affected by modulation when the intensity of the processed echo is static. We can obtain the following round-trip transmission coefficient:

$$\begin{aligned} \mathcal{G}_r(t) &= \frac{E_c'(t)}{E_c(t)} \\ &= r_1 r_2 t_s p^2 \eta_d^2 G^2. \end{aligned} \tag{28}$$

When $\mathcal{G}_r(t) = 1$, the steady state is achieved. In the steady state, no matter what the source signal is, and whether the communication process starts or not, the gain of the gain medium is a constant value, namely

$$G = \frac{1}{p \eta_d \sqrt{r_1 r_2 t_s}}. \tag{29}$$

Here, the dc bias p determines the modulator's transmission coefficient η_m in (13). According to (29), p affects the steady-state gain G.

E. Numerical Examples

In this section, the performance of the interference-free RBCom system is studied. The capacity C and the carrier amplitude A_c are evaluated. Since coherent demodulation is adopted, the channel capacity can be obtained as

$$C = \log_2(1 + \mathrm{SNR}) \tag{30}$$

where

$$\mathrm{SNR} = \frac{\left\langle i_s^2(t) \right\rangle}{\left(\sigma_{\mathrm{shot}}^2 + \sigma_{\mathrm{thermal}}^2\right)/4} \tag{31}$$

where σ_{shot}^2 and $\sigma_{\mathrm{thermal}}^2$ are the power of the shot noise and the thermal noise of PD, respectively. From (24), the average signal power expressed in A^2 is obtained by

$$\left\langle i_s^2(t) \right\rangle = k^2 r_s^4 \eta_d^4 A_c^4 p^2 m^2 \left\langle x^2(t) \right\rangle. \tag{32}$$

The bandwidth of the PD is $2B_x$ which is equal to the BPF at the demodulation circuit. The shot noise power expressed in A^2 is given by

$$\sigma_{\mathrm{shot}}^2 = 2q\left(I_{\mathrm{sig}} + I_{\mathrm{bk}}\right) \times 2B_x \tag{33}$$

where q is electron charge, and I_{sig} and I_{bk} are the photocurrents induced by the signal and the background radiations, respectively. The thermal noise power expressed in A^2 is given by

$$\sigma_{\mathrm{thermal}}^2 = \frac{4KT}{R_L} \times 2B_x \tag{34}$$

where T is the temperature in Kelvin and K is the Boltzmann constant, and $R_L = 10\ \mathrm{k}\Omega$ is the load resistor [32].

The PD's responsivity is $\rho = 0.6$ A/W and its area is 1 cm^2 [33]. As the beam radius is at the level of millimeter, we assume all the beam energy is focused onto the PD by lens, i.e., $\eta_{\mathrm{det}} = 1$. We set $r_1 = r_2 = 1$ and $T = 298$ K. Since well-coated optical components generally have ultralow energy absorption, and typical air transmission loss is 0.01 per 100 m, the corresponding loss can be neglected in indoor scenario [30]. The transmission loss coefficient η_d is dominated by diffraction loss factor which is generally greater than 0.9 for multiple-transverse-mode operation [34]. Hence, we set the transmission coefficient $\eta_d \approx \eta_{\mathrm{diff}} = 0.949$. We assume that $<x^2(t)> = 0.3$. The background radiation induced photocurrent $I_{\mathrm{bk}} = 5100\ \mu$A [35]. Multiple quantum wells (MQW) modulator can support rates up to tens of gigahertz [36]. Hence, we set $B_x = 5$ GHz.

One can assume that the pump power is a fixed value, namely, $P_{\mathrm{in}} = 30$ W. In this case, the carrier amplitude A_c is then treated as a variable given by (see the Appendix for details)

$$A_c = \sqrt{\frac{Z_0 I_s \left[\dfrac{\eta P_{\mathrm{in}}}{I_s \mathcal{A}_b} + \ln \sqrt{t_s^2 p^4 \eta_d^4}\right]}{1 - t_s^2 p^4 \eta_d^4}} \tag{35}$$

where I_s is the saturation intensity; η is a combined efficiency in pumping procedure; and $\mathcal{A}_b$ is the cross section area of the gain medium. (We set $\mathcal{A}_b = 7.854 \times 10^{-7}$ m^2, i.e., the diameter is 1 mm.) The saturation intensity I_s is related to the material of the gain medium. Here, we assume neodymium doped yttrium aluminum garnet (Nd:YAG) is employed as the gain medium. The medium's parameters are $I_s = 2.901 \times 10^7$ W/m^2, $\sigma = 2.8 \times 10^{-23}$ m^2, and $\tau_f = 230\ \mu$s. When a Nd:YAG crystal is employed as the gain medium, the wavelength of the pump light is required to be 808 nm (i.e., the pump frequency $f_p \approx 371$ THz), and the wavelength of the stimulated beam is around 1064 nm (i.e., the carrier frequency $f_c \approx 282$ THz). We set $\eta = 0.65$, as the overlap efficiency, the quantum efficiency, and the Stocks factor are 0.9, 0.95, and 0.76, respectively [24].

Fig. 8 plots how the carrier amplitude A_c (left y-axis) as well as the capacity C (right y-axis) varies with the peak amplitude of the source signal m. As m increases (i.e., the dc bias p decreases), A_c decreases gradually. When m approaches 0 or the threshold m_{th}, the capacity C decrease to 0 rapidly. A relatively high capacity can be achieved when m varies in the range between 0 and m_{th}. Furthermore, a smaller reflection coefficient r_s of the splitter supports a greater m_{th}.

Fig. 9 shows the carrier amplitude A_c as a function of the reflection coefficient r_s of the splitter (left y-axis); and also the capacity C as a function of r_s (right y-axis). As r_s increases,

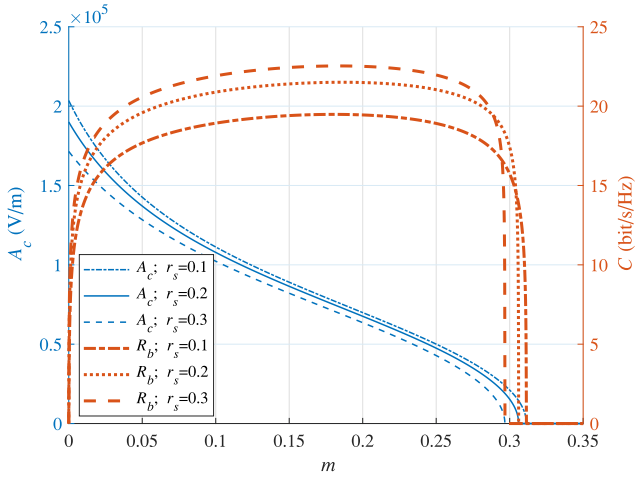

Fig. 8. Carrier amplitude A_c and capacity C versus peak amplitude m of source signal.

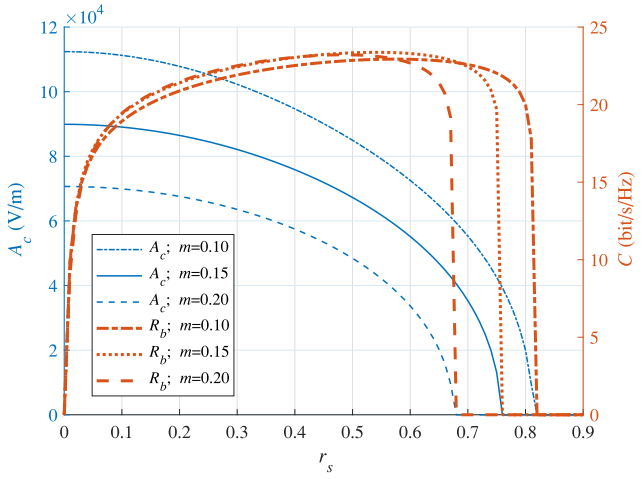

Fig. 9. Carrier amplitude A_c and capacity C versus splitter's reflection coefficient r_s.

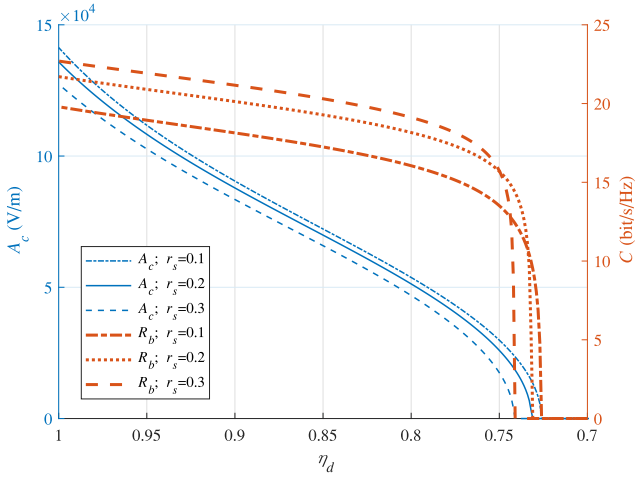

Fig. 10. Carrier amplitude A_c and capacity C versus spatial transmission coefficient η_d (peak source signal amplitude $m = 0.1$).

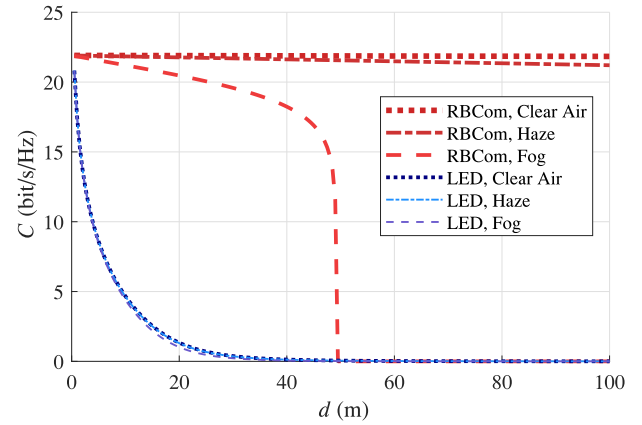

Fig. 11. Comparison between the RBCom system and the LED-based system.

A_c decreases gradually, while C raises. However, when r_s approaches the threshold $r_{s,\text{th}}$, A_c as well as C decrease to 0 rapidly, because the total loss in the cavity becomes greater than the gain. Clearly from Fig. 9, a smaller m (i.e., a greater dc bias p) leads to a greater $r_{s,\text{th}}$.

As demonstrated in Fig. 10, the spatial transmission coefficient η_d also affects the carrier amplitude A_c (left y-axis) and the capacity C (right y-axis). Here, m is set to 0.1. With the decrease of η_d, both A_c and C decrease gradually. The decrease rate of C is small when η_d is great. Nevertheless, when η_d approaches the threshold $\eta_{d,\text{th}}$, A_c as well as C decrease to 0 rapidly.

Next, we compare the performance of the RBCom system with that of the LED-based communication system. We only consider the case where the radiation angle and the incidence angle are zero. According to the LED-based communication channel model presented in [7] and [37], the detected current is obtained as

$$I_{\text{sig,LED}} = \frac{\rho \mathcal{A}_r (m+1)}{2\pi d^2} \frac{n^2}{\sin^2 \Psi_c} T_s e^{-\alpha d} P_t \tag{36}$$

where $\mathcal{A}_r$ is the receiving area, $m = -\ln 2 / \ln(\cos \Phi_{1/2})$ is the order of Lambertian emission, $\Phi_{1/2}$ is the semi-angle (at half power) of the LED, n is the refractive index of a lens at the PD, Ψ_c is the width of the field of vision at the receiver, T_s is the gain of an optical filer, and P_t is the transmit power. Thus, the SNR at the receiver of a LED-based system is

$$\text{SNR}_{\text{LED}} = \frac{I^2_{\text{sig, LED}}}{2q\big(I_{\text{sig,LED}} + I_{\text{bk}}\big)B_x + 4KTB_x/R_L}. \tag{37}$$

Then, the channel capacity of the LED-based system can be obtained by (30). Here, we set $P_t = 30$ W, $\mathcal{A}_r = 1$ cm^2, $n = 1.5$, $T_s = 1$, $\Phi_{1/2} = 70°$, and $\Psi_c = 60°$ [37]. We also assume that the radii of the elements of the RBCom system are great enough so that multiple-transverse-mode operation is assured. As shown in Fig. 11, the RBCom channel capacity decreases slowly as the distance increases, but it decreases rapidly as the distance approaches the threshold. The capacities of the RBCom channels are greater than that of the LED-based communication channel under different air conditions, including clear air, haze, and fog.

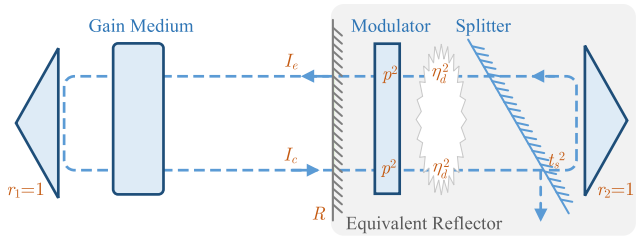

Fig. 12. Equivalent model for computing the carrier amplitude.

VI. Conclusion

In this article, the echo interference mechanism of the RBCom system was at first discussed. Then, the method of interference elimination was proposed, along with an exemplary design based on optical filtering and frequency shifting. We also presented the mathematical model and performance analysis of the exemplary system. Taking account for the impacts, such as transverse mode distribution, phase variation, and pump power fluctuation is worthy of investigating for future work.

Appendix
Derivation of the Carrier Amplitude

To obtain the carrier amplitude A_c, we need to compute the light intensity of the carrier I_c. Here, an equivalent model of the proposed interference-free RBCom system is depicted in Fig. 12. In this model, all the devices on the right-hand side of the gain medium are modeled as a partial reflector. Let I_e denote the intensity of the reflected beam, the intensity reflectivity of the equivalent reflector is derived as

$$R = \frac{I_e}{I_c} = t_s^2 p^4 \eta_d^4. \tag{38}$$

In the equivalent model, the OBPF is neglected, as it imposes less attenuation on the carrier. Besides, we have made the assumption $r_1 = r_2 = 1$ for this system. According to (28), the dc bias p which specifies the operating point of the modulator is regarded as the modulator's amplitude attenuation coefficient η_m. Hence, the two-pass intensity attenuation coefficient of the modulator is p^4, the two-pass intensity attenuation coefficient of transmission is η_d^4, and the intensity transmittance of the splitter is t_s^2.

The equivalent model is a classic laser cavity, and its output power is given by [38]

$$P_{\text{out}} = \frac{\mathcal{A}_b I_s \left[(g_0 - \alpha_0) l + \ln \sqrt{R} \right]}{1 - \dfrac{\alpha_0 l}{\ln \sqrt{R}}} \tag{39}$$

where $\mathcal{A}_b$ is the beam cross section area (for multiple-transverse-mode operation, the cross section area of the laser beam is approximate to that of the gain medium), and α_0 is the loss coefficient of the gain medium. Generally, α_0 is very small compared with the small-signal gain factor g_0, so we set $\alpha_0 = 0$. As the intensity transmittance of the equivalent reflector is $(1 - R)$, the carrier intensity is deduced as

$$I_c = \frac{P_{\text{out}}}{\mathcal{A}_b (1 - R)} = \frac{I_s \left[g_0 l + \ln \sqrt{R} \right]}{1 - R}. \tag{40}$$

Therefore, the carrier amplitude is obtained as

$$A_c = \sqrt{Z_0 I_c} = \sqrt{\frac{Z_0 I_s \left[g_0 l + \ln \sqrt{R} \right]}{1 - R}}. \tag{41}$$

The saturation intensity is given by [24]

$$I_s = \frac{h f_c}{\sigma \tau_f} \tag{42}$$

where h is Planck's constant, and f_c is the carrier beam frequency. The small-signal gain coefficient is given by [24]

$$g_0 = \frac{\sigma \tau_f \eta P_{\text{in}}}{h f_c V} = \frac{\eta P_{\text{in}}}{I_s V} \tag{43}$$

where V is the volume of the gain medium. Here, we assume that the gain medium is a rod or disk with a cross section area $\mathcal{A}_b$ and a length l. Then, we obtain

$$g_0 l = \frac{\eta P_{\text{in}}}{I_s \mathcal{A}_b}. \tag{44}$$

Finally, substituting (38), (42), and (44) into (41) gives

$$A_c = \sqrt{\frac{Z_0 I_s \left[\dfrac{\eta P_{\text{in}}}{I_s \mathcal{A}_b} + \ln \sqrt{t_s^2 p^4 \eta_d^4} \right]}{1 - t_s^2 p^4 \eta_d^4}}. \tag{45}$$

References

[1] M. Xiong, Q. Liu, G. Wang, G. B. Giannakis, S. Zhang, and C. Huang, "Analytical models for resonant beam communications," in *Proc. 11th Int. Conf. Wireless Commun. Signal Process. (WCSP)*, Xi'an, China, 2019, pp. 1–6.

[2] K. David and H. Berndt, "6G vision and requirements: Is there any need for beyond 5G?" *IEEE Veh. Technol. Mag.*, vol. 13, no. 3, pp. 72–80, Sep. 2018.

[3] F. Deng, X. Yue, X. Fan, S. Guan, Y. Xu, and J. Chen, "Multisource energy harvesting system for a wireless sensor network node in the field environment," *IEEE Internet Things J.*, vol. 6, no. 1, pp. 918–927, Feb. 2019.

[4] H. Wang, J. Wang, G. Ding, J. Chen, Y. Li, and Z. Han, "Spectrum sharing planning for full-duplex UAV relaying systems with underlaid D2D communications," *IEEE J. Sel. Areas Commun.*, vol. 36, no. 9, pp. 1986–1999, Sep. 2018.

[5] A. Sadeghi, G. Wang, and G. B. Giannakis, "Deep reinforcement learning for adaptive caching in hierarchical content delivery networks," *IEEE Trans. Cogn. Commun. Netw.*, vol. 5, no. 4, pp. 1024–1033, Dec. 2019.

[6] C. Sun, X. Gao, J. Wang, Z. Ding, and X. Xia, "Beam domain massive MIMO for optical wireless communications with transmit lens," *IEEE Trans. Commun.*, vol. 67, no. 3, pp. 2188–2202, Mar. 2019.

[7] J. M. Kahn and J. R. Barry, "Wireless infrared communications," *Proc. IEEE*, vol. 85, no. 2, pp. 265–298, Feb. 1997.

[8] D. Killinger, "Free space optics for laser communication through the air," *Opt. Photon. News*, vol. 13, no. 10, pp. 36–42, Oct. 2002.

[9] A. Al-Kinani, C. Wang, L. Zhou, and W. Zhang, "Optical wireless communication channel measurements and models," *IEEE Commun. Surveys Tuts.*, vol. 20, no. 3, pp. 1939–1962, 3rd Quart., 2018.

[10] A. D. Yalcinkaya, H. Urey, D. Brown, T. Montague, and R. Sprague, "Two-axis electromagnetic microscanner for high resolution displays," *J. Microelectromech. Syst.*, vol. 15, no. 4, pp. 786–794, Aug. 2006.

[11] K. Wang, A. Nirmalathas, C. Lim, and E. Skafidas, "High-speed optical wireless communication system for indoor applications," *IEEE Photon. Technol. Lett.*, vol. 23, no. 8, pp. 519–521, Apr. 2011.

[12] T. Koonen, J. Oh, K. Mekonnen, Z. Cao, and E. Tangdiongga, "Ultra-high capacity indoor optical wireless communication using 2D-steered pencil beams," *J. Lightw. Technol.*, vol. 34, no. 20, pp. 4802–4809, Oct. 15, 2016.
[13] A. Gomez, K. Shi, C. Quintana, G. Faulkner, B. C. Thomsen, and D. O'Brien, "A 50 Gb/s transparent indoor optical wireless communications link with an integrated localization and tracking system," *J. Lightw. Technol.*, vol. 34, no. 10, pp. 2510–2517, May 15, 2016.
[14] P. Niger and P. Vandamme, "Performance of equalization techniques in a radio interference environment," *IEEE Trans. Commun.*, vol. 39, no. 3, pp. 452–457, Mar. 1991.
[15] Q. Liu *et al.*, "Charging unplugged: Will distributed laser charging for mobile wireless power transfer work?" *IEEE Veh. Technol. Mag.*, vol. 11, no. 4, pp. 36–45, Dec. 2016.
[16] W. Wang, Q. Zhang, H. Lin, M. Liu, X. Liang, and Q. Liu, "Wireless energy transmission channel modeling in resonant beam charging for IoT devices," *IEEE Internet Things J.*, vol. 6, no. 2, pp. 3976–3986, Apr. 2019.
[17] Q. Zhang, G. Wang, J. Chen, G. B. Giannakis, and Q. Liu, "Mobile energy transfer in Internet of Things," *IEEE Internet Things J.*, vol. 6, no. 5, pp. 9012–9019, Oct. 2019.
[18] F. Deng *et al.*, "Energy-based sound source localization with low power consumption in wireless sensor networks," *IEEE Trans. Ind. Electron.*, vol. 64, no. 6, pp. 4894–4902, Jun. 2017.
[19] H. Yang, Y. Ye, X. Chu, and M. Dong, "Resource and power allocation in SWIPT enabled device-to-device communications based on a non-linear energy harvesting model," *IEEE Internet Things J.*, early access, Apr. 17, 2020, doi: 10.1109/JIOT.2020.2988512.
[20] X. Liu *et al.*, "Adaptive data and verified message disjoint security routing for gathering big data in energy harvesting networks," *J. Parallel Distrib. Comput.*, vol. 135, pp. 140–155, Jan. 2020.
[21] H. Li, K. Ota, and M. Dong, "Energy cooperation in battery-free wireless communications with radio frequency energy harvesting," *ACM Trans. Embedded Comput. Syst.*, vol. 17, no. 2, pp. 2–17, Feb. 2018.
[22] G. J. Linford, E. R. Peressini, W. R. Sooy, and M. L. Spaeth, "Very long lasers," *Appl. Opt.*, vol. 13, no. 2, pp. 379–390, Feb. 1974.
[23] G. J. Linford and L. W. Hill, "Nd:YAG long lasers," *Appl. Opt.*, vol. 13, no. 6, pp. 1387–1394, Jun. 1974.
[24] W. Koechner, *Solid-State Laser Engineering, 6th ed.*. New York, NY, USA: Springer, 2006.
[25] S. Junique, D. Agren, Q. Wang, S. Almqvist, B. Noharet, and J. Y. Andersson, "A modulating retro-reflector for free-space optical communication," *IEEE Photon. Technol. Lett.*, vol. 18, no. 1, pp. 85–87, Jan. 2006.
[26] J. Öhgren *et al.*, "A high-speed modulated retro-reflector communication link with a transmissive modulator in a cat's eye optics arrangement," in *Proc. Unmanned/Unattended Sens. Sens. Netw. IV*, vol. 6736. Florence, Italy, Oct. 2007, Art. no. 673619.
[27] F. E. P. Arellano and C. C. Speake, "Mirror tilt immunity interferometry with a cat's eye retroreflector," *Appl. Opt.*, vol. 50, no. 7, pp. 981–991, Mar. 2011.
[28] M. Xiong, Q. Liu, G. Wang, G. B. Giannakis, and C. Huang, "Resonant beam communications: Principles and designs," *IEEE Commun. Mag.*, vol. 57, no. 10, pp. 34–39, Oct. 2019.
[29] O. Svelto, *Principles of Lasers*. New York, NY, USA: Springer, 1982.
[30] I. I. Kim, B. Mcarthur, and E. J. Korevaar, "Comparison of laser beam propagation at 785 nm and 1550 nm in fog and haze for optical wireless communications," *Proc. Spie*, vol. 4214, no. 2, pp. 26–37, Feb. 2001.
[31] Y. Amnon, *Optical Electronics in Modern Communications, Fifth Edition*. New York, NY, USA: Oxford Univ. Press, 1997.
[32] F. Xu, M. Khalighi, and S. Bourennane, "Impact of different noise sources on the performance of PIN- and APD-based FSO receivers," in *Proc. 11th Int. Conf. Telecommun.*, Graz, Austria, Jun. 2011, pp. 211–218.
[33] M. S. Demir, F. Miramirkhani, and M. Uysal, "Handover in VLC networks with coordinated multipoint transmission," in *Proc. IEEE Int. Black Sea Conf. Commun. Netw. (BlackSeaCom)*, Istanbul, Turkey, Jun. 2017, pp. 1–5.
[34] N. Hodgson and H. Weber, *Laser Resonators and Beam Propagation Fundamentals, Advanced Concepts, Applications*. New York, NY, USA: Springer, 2005.
[35] A. J. C. Moreira, T. V. Rui, and A. M. D. O. Duarte, "Optical interference produced by artificial light," *Wireless Netw.*, vol. 3, no. 2, pp. 131–140, May 1997.
[36] G. C. Gilbreath *et al.*, "Modulating retroreflector architecture using multiple quantum wells for free-space optical communications," in *Proc. Int. Conf. Appl. Photon. Technol. III, Closing Gap Theory Develop. Appl.*, vol. 3491. Ottawa, ON, Canada, Dec. 1998, pp. 581–586.
[37] T. Komine and M. Nakagawa, "Fundamental analysis for visible-light communication system using LED lights," *IEEE Trans. Consum. Electron.*, vol. 50, no. 1, pp. 100–107, Feb. 2004.
[38] W. Rigrod, "Homogeneously broadened CW lasers with uniform distributed loss," *IEEE J. Quantum Electron.*, vol. 14, no. 5, pp. 377–381, May 1978.

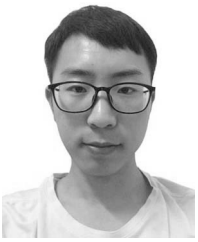

Mingliang Xiong received the B.S. degree in communication engineering from Nanjing University of Posts and Telecommunications, Nanjing, China, in 2017. He is currently pursuing the Ph.D. degree with the College of Electronics and Information Engineering, Tongji University, Shanghai, China.

His research interests include wireless power transfer, simultaneous wireless information and power transfer, and Internet of Things.

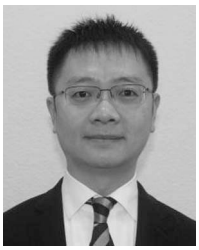

Qingwen Liu (Senior Member, IEEE) received the B.S. degree in electrical engineering and information science from the University of Science and Technology of China, Hefei, China, in 2001, and the M.S. and Ph.D. degrees from the Department of Electrical and Computer Engineering, University of Minnesota, Minneapolis, MN, USA, in 2003 and 2006, respectively.

He is currently a Professor with the College of Electronics and Information Engineering, Tongji University, Shanghai, China. His research interests lie in the areas of wireless power transfer and Internet of Things.

Gang Wang (Member, IEEE) received the B.Eng. degree in electrical engineering and automation from Beijing Institute of Technology, Beijing, China, in 2011, and the Ph.D. degree in electrical engineering from the University of Minnesota, Minneapolis, MN, USA, in 2018.

He was a Postdoctoral Associate with the University of Minnesota from 2018 to 2020. His research interests focus on the areas of signal processing, control, and machine learning with applications to data science and smart grids.

Dr. Wang received the Paper Awards at the 2017 European Signal Processing Conference and the 2019 IEEE Power & Energy Society General Meeting, as well as the Excellent Doctoral Dissertation Award from the Chinese Association of Automation in 2019. He is currently on the editorial board of *Signal Processing*.

Georgios B. Giannakis (Fellow, IEEE) received the Diploma degree in electrical engineering from the National Technical University of Athens, Athens, Greece, in 1981, and the M.Sc. degree in electrical engineering, the M.Sc. degree in mathematics, and the Ph.D. degree in electrical engineering from the University of Southern California, Los Angeles, CA, USA, in 1983, 1986, and 1986, respectively.

He was a Faculty Member with the University of Virginia, Charlottesville, VA, USA, from 1987 to 1998, and since 1999, he has been a Professor with the University of Minnesota, Minneapolis, MN, USA, where he holds an ADC Endowed Chair, a University of Minnesota McKnight Presidential Chair of ECE, and serves as the Director of the Digital Technology Center. His general interests span the areas of statistical learning, communications, and networking—subjects on which he has published more than 465 journal papers, 765 conference papers, 25 book chapters, two edited books, and two research monographs. He is the (co-) inventor of 33 issued patents. His current research focuses on data science, and network science with applications to the Internet of Things, and power networks with renewables.

Dr. Giannakis is the (co-) recipient of nine best journal paper awards from the IEEE Signal Processing and Communications Societies, including the G. Marconi Prize Paper Award in Wireless Communications. He also received the IEEE SPS Nobert Wiener Society Award in 2019; the EURASIP's A. Papoulis Society Award in 2020; the Technical Achievement Awards from the IEEE-SPS in 2000 and from EURASIP in 2005; the IEEE ComSoc Education Award in 2019; the G. W. Taylor Award for Distinguished Research from the University of Minnesota; and the IEEE Fourier Technical Field Award in 2015. He is a Foreign Member of Academia Europaea, and a Fellow of the National Academy of Inventors, the European Academy of Sciences, and EURASIP. He has served the IEEE in a number of posts, including that of a Distinguished Lecturer for the IEEE-SPS.

Sihai Zhang (Senior Member, IEEE) received the Ph.D. degree from the Department of Computer Science and Technology, University of Science and Technology of China (USTC), Hefei, China, in 2006.

He has been with the Key Laboratory of Wireless-Optical Communications, USTC, where he is currently an Associate Professor with the Department of Electronic Engineering and Information Science. He has authored or coauthored over 60 technical articles, such as the IEEE TRANSACTIONS ON EMERGING TOPICS IN COMPUTING, the IEEE TRANSACTIONS ON VEHICULAR TECHNOLOGY, MONET, and WPC. He initiated the research field of wireless big data in 2014. He has participated in many projects, including the National Science Foundation of China for Machine Type Communications and the Key Program of the National Natural Science Foundation of China for Wireless Big Data. His research interests include wireless communication and networks, big data analysis, and machine learning.

Dr. Zhang has been co-organizing five annual workshops on Wireless Big Data since 2014. He has served over 15 international conferences, as a member of organizing committee, a TPC member, or a reviewer, such as the Publication Chair for WCSP 2014. In 2016, he co-chaired special sessions on Wireless Big Data in WCSP 2016 and Machine Type Communications in WPMC 2016. He has been a Guest Editor of Special Issue on Wireless Big Data of JCIN and on Recent Advances in Ultra Dense 5G Networks with Application to Machine Type Communication of IJDSN in 2017.

Jinkang Zhu (Life Member, IEEE) received the B.S. degree in electrical engineering from Sichuan University, Chengdu, China, in 1966.

He joined the University of Science and Technology of China, Hefei, China, in 1966, where he has been a Professor since 1992. He has been committed to research on wireless mobile communications and networks, signal processing for communications, and the future wireless technologies.

Chuan Huang (Member, IEEE) received the Ph.D. degree in electrical engineering from Texas A&M University, College Station, TX, USA, in 2012.

From August 2012 to July 2014, he was a Research Associate and then a Research Assistant Professor with Arizona State University, Tempe, AZ, USA, and Princeton University, Princeton, NJ, USA, respectively. He is currently an Associate Professor with the Chinese University of Hong Kong, Shenzhen, China. His current research interests include wireless communications and signal processing.

Dr. Huang served as a Symposium Chair of IEEE GLOBECOM 2019 and IEEE ICCC 2019 and 2020. He is currently serving as an Editor for the IEEE TRANSACTIONS ON WIRELESS COMMUNICATIONS, IEEE ACCESS, the *Journal of Communications and Information Networks*, and IEEE WIRELESS COMMUNICATIONS LETTERS.